Optics Letters

Engineering third-order optical nonlinearities in hybrid chalcogenide-on-silicon platform

Samuel Serna,[1,2,*] Hongtao Lin,[2] Carlos Alonso-Ramos,[1] Christian Lafforgue,[1] Xavier Le Roux,[1] Kathleen A. Richardson,[3] Eric Cassan,[1] Nicolas Dubreuil,[4,5] Juejun Hu,[2] and Laurent Vivien[1]

[1]Centre de Nanosciences et de Nanotechnologies (C2N), CNRS, Univ. Paris-Sud, Université Paris Saclay, C2N, 91120, Palaiseau, France
[2]Department of Materials Science and Engineering, Massachusetts Institute of Technology, Cambridge, Massachusetts 02139, USA
[3]College of Optics and Photonics-CREOL, University of Central Florida, Orlando, Florida 32816, USA
[4]Laboratoire Charles Fabry, Institut d'Optique Graduate School, CNRS, Université Paris Saclay, 2 Avenue Augustin Fresnel, 91127 Palaiseau cedex, France
[5]Current address: LP2N, Institut d'Optique Graduate School, CNRS, Univ. Bordeaux, 33400 Talence, France
*Corresponding author: safes@mit.edu

Received 23 July 2019; revised 11 September 2019; accepted 12 September 2019; posted 13 September 2019 (Doc. ID 373158); published 10 October 2019

We demonstrated a class of highly nonlinear hybrid waveguide structures based on infiltration of As_2S_3 chalcogenide glass into silicon slot waveguides. The nonlinear properties of the hybrid waveguides were precisely quantified via a bidirectional top-hat D-scan method, enabling a direct comparison between properties measured using different device geometries. We experimentally demonstrate hybrid As_2S_3-Si slot waveguides with a two-photon absorption (TPA) figure of merit exceeding 2 at near infrared wavelengths. These waveguides largely satisfy the critical criterion for efficient nonlinear integrated photonics ($FOM_{TPA}^{wg} > 1$), allowing phase shifts greater than π with minimal overall losses. These results pave the way for efficient and robust ultrafast all-optical devices and circuits in large-scale silicon photonics technology.

https://doi.org/10.1364/OL.44.005009

Optical communications are at the core of the internet today, enabling the development of the interconnected modern society. However, in order to meet the requirements of future communication system applications, optical circuits have to be faster, smaller, less power hungry, and more cost-effective, while delivering ever-growing data rates. Silicon photonics, due to its compatibility with standard CMOS fabrication processes, is uniquely positioned to enable ultracompact optoelectronic chips meeting these requirements [1]. In recent years, the silicon photonics community has developed the key building blocks including passive devices, modulators [2], optical isolators [3], and germanium photodetectors [4], along with III–V lasers on silicon [5]. This groundbreaking family of optical devices are delivering high-speed data communication solutions for data centers and high-performance computers today. Nonetheless, the problem of bandwidth scalability remains unsolved, posing a significant challenge and limiting further advances. While optical fibers can readily transport hundreds of optical carriers at different wavelengths to reach petabit/s aggregate data rates, implementing a multiwavelength communication system to extend this level in integrated Si photonics circuits presents a significant challenge. The ever-growing bandwidth demand is therefore mandating ultrafast all-optical solutions based on both materials and processing methodologies.

A promising route to satisfy this demand is to exploit optical nonlinearities to realize such ultrafast all-optical devices. Several interesting demonstrations have been reported by exploiting third-order nonlinearities in on-chip devices, such as all-optical regeneration [6] and heralded single-photon sources [7]. Even though silicon, the master material for integrated photonics, exhibits a remarkably large Kerr nonlinear coefficient, it also suffers from very high two-photon absorption (TPA) in the C and L telecom bands [8]. The medium's nonlinear loss strongly limits the efficiency of ultrafast all-optical devices based entirely on Si. For instance, TPA-induced losses are the primary attribute limiting the attainable ultrafast nonlinear phase shift. At the same time, TPA also generates free carriers that change the refractive index and absorption of the guiding material, resulting in a much slower parasitic nonlinear response. The relative magnitude of the desired ultrafast optical Kerr effect and the deleterious TPA is usually quantified, in bulk materials, by a figure of merit $FOM_{TPA}^{bulk} = n_2/(\beta_{TPA}\lambda)$, with n_2 denoting the nonlinear refractive index, and β_{TPA} representing the TPA coefficient and λ the pump wavelength. This expression takes a different form when considering waveguiding structures, $FOM_{TPA}^{wg} = \mathrm{Re}(\gamma^{wg})/(4\pi\mathrm{Im}(\gamma^{wg}))$, where γ^{wg} is the effective nonlinear third-order susceptibility that takes into account the effects of the waveguide geometry [9] and the nonlinear contribution of different materials [10].

One way to mitigate the impact of nonlinear losses while still taking advantage of the scalable manufacturing of silicon

is to use a slot waveguide configuration. In a slot waveguide, light is confined within a gap between semiconductor rails by taking advantage of the high permittivity contrast between Si and the slot medium [11]. The use of such hollow core structures where the slot contains air or other materials is further extended with the possibility of integrating diverse materials such as doped polymers, glasses, and other semiconductors into the slot to achieve unconventional thermal, optical, or electronic attributes and functionality, not attainable with Si alone.

The use of such hybrid slot waveguide structures for a novel nonlinear photonics platform has garnered a considerable interest in the recent years [12]. To date, most work in this area has utilized organic materials such as DDMEBT [13,14] and p-toluene sulphonate (PTS) [15] to improve the effective nonlinearities. Chalcogenide glasses (ChGs) represent another class of promising nonlinear optical material for high FOM_{TPA} hybrid silicon structures. It has been known from prior studies on bulk and waveguides fabricated in ChGs that these compositionally tailorable materials have a significantly lower TPA coefficient and potentially higher nonlinear refractive indices than silicon [16]. Even simple strip silicon waveguides covered with ChGs have demonstrated the potential to considerably boost the third-order nonlinear figure of merit [17]. A Si-ChG hybrid slot waveguide would be expected to exhibit a superior nonlinear device platform benefiting from the high FOM_{TPA} of ChGs and the strong field confinement in the slot region.

There are, however, a number of fabrication challenges involved in manufacturing the proposed hybrid slot waveguides, most significantly, homogeneous infiltration of the nanoscale slot with the ChG materials [18]. Optimizing the waveguide processing protocol to minimize linear optical loss caused by scattering due to roughness at the slot region [19,20] and the design of the waveguide linear and nonlinear propagation parameters are among other potential technical challenges. Moreover, precise quantification of nonlinear susceptibilities and the figure of merit in the spectral range of use for the hybrid devices is essential to demonstrate their advantage relative to standard Si waveguides.

In this Letter, we demonstrate experimentally complete and homogeneous filling of the nanoslot in silicon waveguides with As_2S_3 glass using a simple thermal reflow process. We also validate enhancement of third-order nonlinearities and the nonlinear figure of merit in the hybrid slot waveguides using a bidirectional D-scan measurement method [21], showing the possibility of engineering effective nonlinearities in complex hybrid photonic circuits. We show experimentally that it is possible to have different effective nonlinearities by changing the slot's geometry. Our result illustrates for the first time the potential for the development of dispersion engineered slotted structures [10] for efficient ultrafast all-optical nonlinear photonics in chip-scale platforms.

The devices were fabricated on silicon on insulator (SOI) wafers with a 220-nm-thick silicon layer over 2 μm of buried SiO_2. Device structures (slots) were defined in ZEP-520A resist (Zeon Chemical Co.) by an 80 kV e-beam lithography nanobeam NB-4 system. The writing field was set to $50 \times 50\ \mu m^2$ for a beam current of 0.5 nA and a beam step size of 2 nm. The resist patterns were then transferred to the Si layer by an inductively coupled plasma (ICP) reactive ion etching process using SF_6 and C_4F_8 gases. Following this, thin films of As_2S_3 were prepared using single-source thermal evaporation. The film deposition was performed using a custom-designed system (PVD Products, Inc.) following previously established protocols [22]. The devices were then annealed for 1 min at 250°C in an inert gas atmosphere. The annealing step reduces viscosity of As_2S_3 at elevated temperatures to facilitate viscous flow of the glass. Since As_2S_3 wets Si waveguide surfaces, the glass can spontaneously fill the slots completely without leaving voids or other loss-inducing defects [23]. Finally, the hybrid samples were mechanically cleaved for optical characterization using free space butt-coupling elements to precisely control the power, dispersion and polarization. Figure 1(a) shows a tilted-view scanning electron micrograph (SEM) image of a strip silicon waveguide partially covered with As_2S_3 glass after annealing. The smoothed film edges are indicative of viscous flow of the material. Figure 1(b) shows the cross-sectional SEM image of a slot waveguide filled with As_2S_3 glass. Here the slot width is 70 nm, and the silicon rail dimensions are 220 nm × 220 nm. The glass completely fills the slot without visible voids or defects.

To investigate the impact of the hybrid waveguide design on the nonlinear parameters, we calculated and plotted in Fig. 2(a)

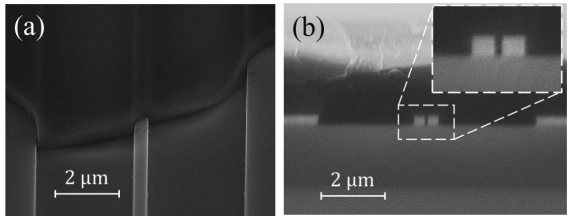

Fig. 1. Hybrid As_2S_3-on-silicon waveguide platform. (a) SEM image of a Si strip waveguide covered with annealed As_2S_3 glass. (b) SEM image of hybrid slot waveguide with 70 nm slot width and 220 nm × 220 nm Si rails, showing complete filling of the slot by As_2S_3 after thermal treatment.

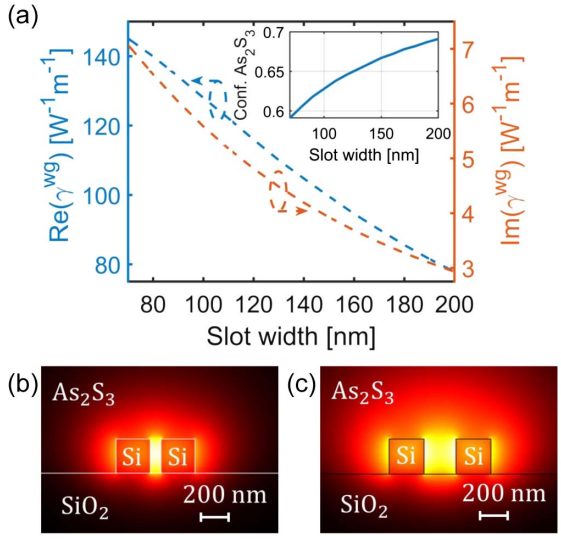

Fig. 2. (a) Simulated modal real (left axis) and imaginary (right axis) effective waveguide nonlinear susceptibility of hybrid As_2S_3-silicon waveguides as a function of slot width. Inset: modal confinement factor in As_2S_3. TE-polarized modal profile for (b) 70 nm and (c) 200 nm slot widths.

the effective nonlinear waveguide susceptibility [9]. For the calculations at telecom wavelengths, we have considered linear refractive indices of $n^{As_2S_3} = 2.4$ and $n^{Si} = 3.5$, nonlinear refractive indices of $n_2^{As_2S_3} = 2.9 \times 10^{-18}$ m^2/W and $n_2^{Si} = 2.0 \times 10^{-18}$ m^2/W, and two-photon absorption coefficients of $\beta_{TPA}^{As_2S_3} = 6.2 \times 10^{-15}$ m/W and $\beta_{TPA}^{Si} = 2.6 \times 10^{-12}$ m/W, corresponding to $FOM_{TPA}^{As_2S_3} = 304$ and $FOM_{TPA}^{Si} = 0.49$ [16,21]. The real (left axis) and imaginary (right axis) magnitudes decrease as the slot width increases, as have been shown in previous simulation works [14]. Nevertheless, the decrease ratio is different for both quantities, being the imaginary part of the effective nonlinear susceptibility more affected. The inset displays the confinement factor in the As_2S_3 cladding, confirming that a larger portion of the field interacts with the overall cladding when increasing the slot size.

In Figs. 2(b) and 2(c), the TE fundamental mode in the hybrid slot waveguide at a wavelength of 1580 nm is displayed for slot widths of 70 nm and 200 nm, respectively. The plots clearly highlight the strong mode confinement in the ChG-filled slot region and the difference between both structures, Fig. 2(b) showing a smaller effective area and Fig. 2(c) showing a larger amount of energy interacting with the cladding material. This means that less power is confined in the silicon rails, decreasing the TPA. Both effects are beneficial to increase the nonlinear interactions and manifest a trade-off for choosing the proper geometrical parameters. Additionally, a smaller slot width results in larger propagation losses due to roughness scattering [20].

Based on these results, we focused our experimental study on the analysis of the impact of two essential device parameters: the slot width and the propagation length of the slot waveguide. Single-mode strip Si waveguides with a semi-standard cross-sectional dimension of 450 nm × 220 nm and similarly cladded with As_2S_3 glass were also included in the study as a reference to confirm that the largest enhancement of the nonlinearities comes from the slot effect. The linear propagation losses for the different slot waveguides were quantified via a cutback method to be 10 ± 2 dB/cm, 15 ± 3 dB/cm, and 16 ± 3 dB/cm for 160 nm, 140 nm, and 110 nm slot sizes, respectively.

To measure the figure of merit of different waveguides, we used our previously developed bidirectional top-hat D-scan technique [21]. As a temporal domain analog of the well-known Z-scan technique, the D-scan method allows direct measurement of the waveguide coupling coefficients as well as the effective real and imaginary nonlinear coefficients. The setup consists of a mode-locked erbium-doped fiber laser that delivers 150 fs duration pulses with a repetition rate of 50 MHz centered at a wavelength of $\lambda = 1580$ nm. After passing through a polarization beam splitter that guarantees the polarization state to excite the fundamental TE mode, the pulses are shaped through a grating-based stretcher that fixes the pulse spectrum following a top-hat shape and introduces an adjustable dispersion coefficient $\phi^{(2)}$. For the structures under test, $\phi^{(2)}$ is between 3 ps^2 and −3 ps^2. For larger dispersion the peak power becomes so small that the nonlinearities are negligible. In the Fourier limit, the autocorrelation pulse duration has been measured to be $T_0 = 2$ ps. The TE polarized beam exiting the stretcher is injected via butt coupling to the waveguide using a microscope objective (20×), which matches the guided mode in the taper. After the sample, another polarization beam splitter is used to verify the transmitted polarization state.

The real and imaginary parts of the effective waveguide susceptibility was measured in the reference waveguide equal to $\mathrm{Im}(\gamma^{ref_{wg}}) = 18 \pm 2$ W^{-1} m^{-1} and $\mathrm{Re}(\gamma^{ref_{wg}}) = 159 \pm 16$ W^{-1} m^{-1}, giving a nonlinear figure of merit $FOM_{TPA} = 0.7 \pm 0.1$ which is 31% higher than in silicon waveguides without a As_2S_3 cladding, found to be 0.48 by using the same technique [21]. This result also allows us to subtract the contributions from the access waveguide connected to the slot waveguide. In fact, by knowing the nonlinear effective susceptibilities in the strip waveguide, it is possible to quantify the nonlinear phase shift prior the slot waveguide by the relation $\phi^{NL} = \mathrm{Re}(\gamma^{wg_{ref}}) \times \ln(1 + 2\mathrm{Im}(\gamma^{wg_{ref}})P_{in}L_{eff})/(2\mathrm{Im}(\gamma^{wg_{ref}}))$, as well as the decrease in the peak power due to TPA with the relation $P_{out} = P_{in}e^{-\alpha L_{eff}}/(1 + 2\mathrm{Im}(\gamma^{wg_{ref}})P_{in}L_{eff})$, where P_{in} is the injected peak power, α the linear propagation losses, and L_{eff} the effective propagation length.

Three different structures with distinct slot widths were subsequently characterized. Figure 3 shows an example of the D-scan curves for the hybrid waveguide with a 160 nm slot width. In agreement with the positive sign of n_2 for silicon and As_2S_3, the maximum root-mean-square linewidth (2σ) is observed in Fig. 3(a) toward positive $\phi^{(2)}$ values [21]. On the other hand, the presence of TPA is evident when the output power is plotted as a function of $\phi^{(2)}$ in Fig. 3(b). The decrease in the output power when the dispersion goes toward zero is a manifestation of the imaginary susceptibility of the silicon rails and access waveguides.

The measurement results and waveguide characteristics are summarized in Table 1. A combination of different slot widths and propagation lengths was used, showing the trend of the larger FOM_{TPA} for the larger slot width. The conclusion is consistent with simulation results shown in Fig. 4, where we plot the simulated FOM_{TPA} values as the dashed purple line. With the increasing slot width, the real nonlinear susceptibility diminishes due to depletion of the slot effect. Meanwhile, the imaginary part of nonlinear susceptibility decreases at a faster pace, as less power is confined in silicon where TPA takes place. Consequently, increasing the slot width leads to a moderate increase of the FOM_{TPA}. This is in agreement with the

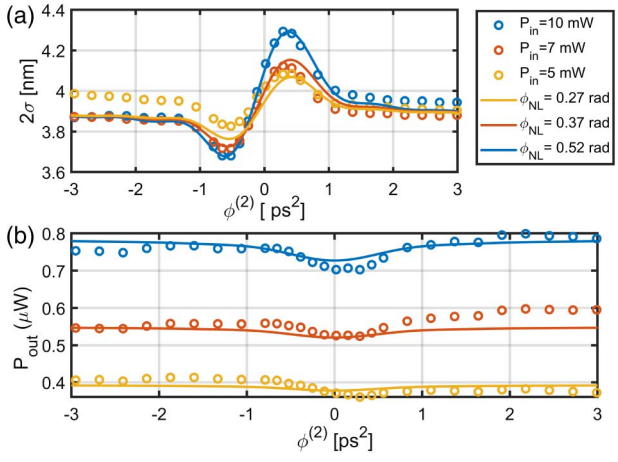

Fig. 3. D-scan characterization of the waveguide with slot size 160 nm and propagation length of 0.85 mm. Measured (open circles) and simulated (solid line) spectral (a) root-mean-squared linewidth (2σ) and (b) output power as a function of the second-order dispersion $\phi^{(2)}$ for three different average input powers.

Table 1. Summary of the Diverse Devices Characterized[a]

Slot Size [nm]	Prop. L^{slot} [mm]	L_{eff}^{slot} [mm]	Re(γ^{slot}) [W^{-1} m^{-1}]	FOM_{TPA}^{wg} –
0	–	–	159 ± 16	0.7 ± 0.1
110 ± 10	1.65	1.37	120 ± 20	1.5 ± 0.5
140 ± 10	0.45	0.42	105 ± 18	1.8 ± 0.6
160 ± 10	0.85	0.73	95 ± 15	2.1 ± 0.7

[a]Different slot sizes, propagation and effective lengths, and figure of merit in the slot waveguide FOM_{TPA}^{wg}.

trend predicted in other simulation studies [14]. Considering that the propagation losses also tend to decrease as the slot width increases, both the simulation and experimental results suggest that waveguides with a wider slot are preferred for nonlinear applications.

Compared to silicon (the gray bar in Fig. 4), the hybrid slot waveguides exhibit a fourfold improvement in terms of the FOM_{TPA}. More importantly, we show that the FOM_{TPA} of all the slot waveguides measured are larger than unity (olive-colored-dashed line in Fig. 4). These devices thus meet a critical criterion for efficient nonlinear integrated photonics. Specifically, the power required to reach a π phase shift for the fabricated device with a 160 nm slot width and a 0.73 mm effective length is on the order of 45 W, the power levels already used in the past with the same chalcogenide glass composition [24]. Moreover, the slot waveguide configuration further enables precise tailoring of the dispersion characteristics [25,26] and enhancement of light–matter interactions with slow light [10].

In conclusion, we demonstrated the improvement of nonlinear properties in hybrid silicon slot waveguides filled with As_2S_3 chalcogenide glass. We have shown that the slot width is a critical design parameter that governs the linear propagation losses, the confinement factor in the slot region, and the figure of merit FOM_{TPA}. We further conclude that larger slot widths are beneficial as they combine lower linear propagation losses and a larger FOM_{TPA}, although they require longer structures as the effective area is larger. Our result opens new opportunities for engineering effective nonlinearities in integrated photonic devices and is useful for realizing novel nonlinear functionalities such as stimulated Brillouin scattering (SBS) [27] and the Kerr effect induced spectral broadening in a silicon-based platform.

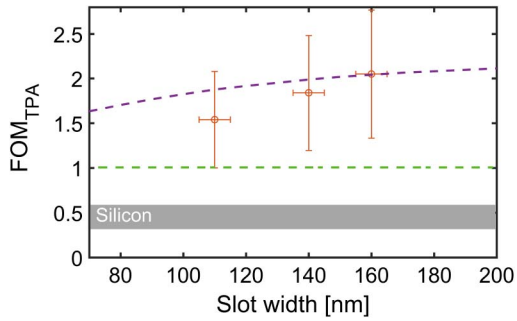

Fig. 4. Simulated TPA figure of merit (FOM_{TPA}) as a function of the slot width (dashed purple line). Experimentally measured values for three different slot widths are also displayed. The olive-colored-dashed horizontal line marks the threshold value of $FOM_{TPA} = 1$, and the gray bar corresponds to the typical FOM_{TPA} range in silicon waveguides.

Funding. H2020 European Research Council (647342); National Science Foundation (1506605); Agence Nationale de la Recherche (MIR-SPEC).

Acknowledgment. The authors thank Philippe Delaye for fruitful discussions.

REFERENCES

1. L. Vivien and L. Pavesi, *Handbook of Silicon Photonics* (Taylor & Francis, 2016).
2. A. Liu, R. Jones, L. Liao, D. Samara-Rubio, D. Rubin, O. Cohen, R. Nicolaescu, and M. Paniccia, Nature **427**, 615 (2004).
3. Q. Du, C. Wang, Y. Zhang, Y. Zhang, T. Fakhrul, W. Zhang, C. Goncalves, C. Blanco, K. Richardson, L. Deng, C. A. Ross, L. Bi, and J. Hu, ACS Photon. **5**, 5010 (2018).
4. L. Vivien, M. Rouvière, J.-M. Fédéli, D. Marris-Morini, J.-F. Damlencourt, J. Mangeney, P. Crozat, L. El Melhaoui, E. Cassan, X. Le Roux, D. Pascal, and S. Laval, Opt. Express **15**, 9843 (2007).
5. J. Justice, C. Bower, M. Meitl, M. B. Mooney, M. A. Gubbins, and B. Corbett, Nat. Photonics **6**, 610 (2012).
6. R. Salem, M. A. Foster, A. C. Turner, D. F. Geraghty, M. Lipson, and A. L. Gaeta, Opt. Express **15**, 7802 (2007).
7. C. A. Husko, A. S. Clark, M. J. Collins, A. De Rossi, S. Combrié, G. Lehoucq, I. H. Rey, T. F. Krauss, C. Xiong, and B. J. Eggleton, Sci. Rep. **3**, 3087 (2013).
8. J. Leuthold, C. Koos, and W. Freude, Nat. Photonics **4**, 535 (2010).
9. C. Koos, L. Jacome, C. Poulton, J. Leuthold, and W. Freude, Opt. Express **15**, 5976 (2007).
10. S. Serna, P. Colman, W. Zhang, X. Le Roux, C. Caer, L. Vivien, and E. Cassan, Sci. Rep. **6**, 26956 (2016).
11. V. R. Almeida, Q. Xu, C. A. Barrios, and M. Lipson, Opt. Lett. **29**, 1209 (2004).
12. M. Li, L. Zhang, L.-M. Tong, and D.-X. Dai, Photon. Res. **6**, B13 (2018).
13. T. Vallaitis, S. Bogatscher, L. Alloatti, P. Dumon, R. Baets, M. L. Scimeca, I. Biaggio, F. Diederich, C. Koos, W. Freude, and J. Leuthold, Opt. Express **17**, 17357 (2009).
14. W. Zhang, S. Serna, N. Dubreuil, and E. Cassan, Opt. Lett. **40**, 1212 (2015).
15. L. An, H. Liu, Q. Sun, N. Huang, and Z. Wang, Appl. Opt. **53**, 4886 (2014).
16. B. J. Eggleton, B. Luther-Davies, and K. Richardson, Nat. Photonics **5**, 141 (2011).
17. A. Zarifi, A. C. Bedoya, B. Morrison, Y. Zhang, G. Ren, T. Nguyen, S. Madden, K. Vu, A. Mitchell, C. Wolff, D. Marpaung, and B. J. Eggleton, in *Nonlinear Photonics* (Optical Society of America, 2016), paper NM4A–6.
18. P. W. Nolte, C. Bohley, and J. Schilling, in *11th International Conference on Group IV Photonics (GFP)* (IEEE, 2014), pp. 118–119.
19. S. R. Mirnaziry, C. Wolff, M. Steel, B. J. Eggleton, and C. G. Poulton, Opt. Express **24**, 4786 (2016).
20. D. M. Kita, J. Michon, S. G. Johnson, and J. Hu, Optica **5**, 1046 (2018).
21. S. Serna and N. Dubreuil, Opt. Lett. **42**, 3072 (2017).
22. Q. Du, Z. Luo, H. Zhong, Y. Zhang, Y. Huang, T. Du, W. Zhang, T. Gu, and J. Hu, Photon. Res. **6**, 506 (2018).
23. J. Hu, N.-N. Feng, N. Carlie, L. Petit, A. Agarwal, K. Richardson, and L. Kimerling, Opt. Express **18**, 1469 (2010).
24. M. R. Lamont, B. Luther-Davies, D.-Y. Choi, S. Madden, and B. J. Eggleton, Opt. Express **16**, 14938 (2008).
25. L. Zhang, Y. Yue, Y. Xiao-Li, J. Wang, R. G. Beausoleil, and A. E. Willner, Opt. Express **18**, 13187 (2010).
26. M. Sinobad, A. Della Torre, B. Luther-Davis, P. Ma, S. Madden, S. Debbarma, K. Vu, D. J. Moss, A. Mitchell, J.-M. Hartmann, J.-M. Fedeli, C. Monat, and C. Grillet, J. Opt. Soc. Am. B **36**, A98 (2019).
27. B. J. Eggleton, C. G. Poulton, and R. Pant, Adv. Opt. Photon. **5**, 536 (2013).